



Simulated solar driven catalytic degradation of psychiatric drug carbamazepine with binary BiVO_4 heterostructures sensitized by graphene quantum dots

Liang Tang^a, Jia-jun Wang^a, Cheng-tao Jia^a, Geng-xin Lv^{a,b}, Gang Xu^a, Wei-tao Li^c, Liang Wang^{c,*}, Ji-ye Zhang^d, Ming-hong Wu^{a,*}

^a Shanghai Institute of Applied Radiation, School of Environmental and Chemical Engineering, Shanghai University, Shanghai 200444, PR China

^b Division of Interfacial Water and Key Laboratory of Interfacial Physics and Technology, Shanghai Institute of Applied Physics, Chinese Academy of Sciences, Shanghai 201800, PR China

^c Institute of Nanochemistry and Nanobiology, School of Environmental and Chemical Engineering, Shanghai University, Shanghai 200444, PR China

^d School of Materials Science and Engineering, Shanghai University, Shanghai 200444, PR China



ARTICLE INFO

Article history:

Received 20 June 2016

Received in revised form 15 October 2016

Accepted 24 October 2016

Available online 25 October 2016

Keywords:

$\text{GQD}/\text{m-BiVO}_4/\text{t-BiVO}_4$

Simulated solar-light

Photocatalysis

Carbamazepine

Mechanisms

ABSTRACT

Herein, solar-driven GQDs loaded BiVO_4 heterostructure catalysts were fabricated and employed to degrade carbamazepine (CBZ) under simulated solar light. The as-prepared ternary catalysts ($\text{GQD}/\text{m-BiVO}_4/\text{t-BiVO}_4$) were thoroughly characterized by TEM, HRTEM, XRD, XPS, UV-vis, Raman and PL. The characterization results demonstrated that GQDs are well-dispersed on binary BiVO_4 support, and the optical properties of the composites are improved with GQDs loaded. The photocatalytic activities of the novel composite catalysts were significantly increased by incorporation of GQDs on original BiVO_4 semiconductor. In particular, the 1.0 wt% GQD loaded catalysts exhibited the highest photocatalytic activity for CBZ, and the mineralization degree of CBZ with the catalysts could achieve more than 95%. In addition, the transformation products (TPs) of CBZ during the catalysis processes were tentatively identified, and hydroxyl radicals were regarded as the predominant active species. From the results of density functional theory (DFT) calculations and evolution of TPs, hydroxylation and cleavage of amide group on the heterocycle may be the main initial photocatalytic degradation channels for CBZ under the catalysis of GQD/BiVO_4 .

© 2016 Published by Elsevier B.V.

1. Introduction

With the improving requirements for clean and safe freshwater, the concerns on the fate of micro-contaminants in aquatic environment have been aroused for a decade [1–3]. Among the conspicuous micropollutants, pharmaceutically active compounds (PhACs) are generally considered as frustrating compounds, since they are continuous input to environment and persistent to the aquatic ecosystem even at low concentrations [4,5]. Moreover, the development of human society and modern medicine constantly push the family scale of PhACs forward. Thus, removing PhAC pollutants from water to guarantee safe water is important and urgent research scope.

Carbamazepine (CBZ), a common used psychiatric drug which was first marketed in 1963, has shared a significant market so far. It was estimated with an annual consumption rate of about 2,235,000 pounds worldwide, and about 77,000 pounds in the US in 2008 [6]. Owing to the large consumption stable and chemical structure of CBZ, this compound continuously introduced into the environment and persistent in environmental mediums through distinct paths. As a persistent PhAC, however, CBZ cannot be effectively removed (<10%) by conventional wastewater treatment plants (WWTPs) as reported [7]. Nevertheless, some studies even showed higher effluent CBZ concentration as compared to influent [8,9]. Consequently, studies have demonstrated CBZ is one of the most frequently detected PhACs in WWTPs and surface water worldwide [10–14], with concentrations up to $\mu\text{g L}^{-1}$ levels in surface water, and dozens of ng L^{-1} in drinking water [15].

In order to remove CBZ residues and eliminate its adverse effects on ecological systems and human bodies, a number of approaches, especially advanced oxidation processes (AOPs) were developed to

* Corresponding authors.

E-mail addresses: wangl@shu.edu.cn (L. Wang), mhwu@shu.edu.cn (M.-h. Wu).

further dispose wastewater containing CBZ to cover the insufficient treatment from WWTPs. The approaches as Fenton oxidation [16], ultraviolet irradiation combining with chemical oxidizers [17] or catalysts [18], ultrasonic irradiation [19], have demonstrated AOPs exhibited higher degradation effects and efficiencies comparing with conventional biological treatment. AOPs are proven as promising technologies toward the treatment and disposal of PhACs such as CBZ. Although there are multi-advantages presented by AOPs, some current existing shortages should not be neglected as well. For instance, those technologies expressing well disposal effect always require the participation of high energy or harsh chemical additives, which may cause not only high operating costs but also output of secondary pollution [20]. Therefore, developing environmentally-friendly and energy sustainable ways more than high efficiency to deal with refractory PhACs is much needed.

To date, the preparations of visible-light catalysts and their applications on heterogeneous catalysis for the removal of organic contaminants in aqueous solutions have made great progresses [21–23]. An appropriate catalyst may not only enhance the eliminated effects on pollutants, but also can reduce the performance costs, and possess potential practical applications. Bismuth vanadate (BiVO_4), as a nontoxic, high chemical stable and visible-light driven catalyst with narrow band gap energy of 2.4 eV ($\lambda < 520 \text{ nm}$), has been demonstrated to be active in photocatalytic oxidation for several dye compounds and studied intensively [24,25]. Recently, research revealed BiVO_4 with heterostructures ($m\text{-BiVO}_4/t\text{-BiVO}_4$) could significantly enhance the catalytic performance comparing with the isolated phase [26]. However, more efforts should be done to improve the catalytic performance to be appropriate for the catalytic degradation of resistant PhAC pollutants. Based on previous researches, the sensitization for catalysts with light-sensitive materials to form heterojunctions was a reasonable way to improve the catalysts' performance [27–29].

Herein, preferably visible-light-sensitive graphene quantum dots (GQDs) were prepared and loaded on BiVO_4 heterostructures. The novel ternary heterojunction catalysts (GQD/ $m\text{-BiVO}_4/t\text{-BiVO}_4$) were then applied to the catalytic degradation of environmentally resistant drug CBZ. The catalytic performance and mechanisms for CBZ with the catalyst under the simulated solar irradiation were studied and evaluated comprehensively.

2. Experimental

2.1. Chemicals and reagents

The precursors used to prepare BiVO_4 , i.e. bismuth nitrate ($\text{Bi}(\text{NO}_3)_3 \cdot 5\text{H}_2\text{O} \geq 99.0\%$), ammonium metavanadate ($\text{NH}_4\text{VO}_3 \geq 99.0\%$) were purchased from Sigma-Aldrich Corp. (MO, USA). CBZ (>98%, purity) and HPLC grade ethanol were also obtained from Sigma-Aldrich Corp. Deionized water (DI, resistance > 18.2 M Ω cm) from a Milli-Q system (Sartorius 611, Germany) was used to prepare all solutions. All glassware was manually cleaned with detergent, acetone, DI, and air-dried before use.

2.2. Synthesis

BiVO_4 heterostructures were synthesized using a hydrothermal process. Specifically, 14.55 g of $\text{Bi}(\text{NO}_3)_3 \cdot 5\text{H}_2\text{O}$ and 3.51 g of NH_4VO_3 were dissolved in 250 mL and 50 mL of nitric acid (2 M) under vigorous stirring at room temperature to obtain $\text{Bi}(\text{NO}_3)_3$ solution and NH_4VO_3 solution, respectively. Then NH_4VO_3 was dropwise added into $\text{Bi}(\text{NO}_3)_3$ solution. The obtained solution was then sufficiently mixed for 2 h, followed by adjusting solution pH to 2 with ammonia, then transferred into a poly(tetrafluoroethylene)

(Teflon)-lined autoclave and heated at 200 °C for 24 h. The mixture was allowed to cool down to room temperature, filtrated using filter paper. The solid fractions were washed with DI and ethanol several times, and then dried under vacuum at 80 °C.

The synthesis method of GQDs was described in our previous studies published elsewhere [30,31]. Then, GQD/ BiVO_4 heterojunctions were prepared by mixing GQDs and BiVO_4 through a hydrothermal method. Specifically, to obtain 1.0 wt%-GQD/ BiVO_4 composites, 0.1 g BiVO_4 nanowires were added into 10 mL of GQD solution (0.1 mg mL $^{-1}$) with stir-ring for 1 h at room temperature to obtain a homogeneous suspension. After that, the suspension was transferred into apoly(tetrafluoroethylene) (Teflon)-lined autoclave (100 mL) and maintained at 150 °C for 4 h, and dried at 80 °C, followed by annealing at 250 °C in N_2 for 4 h to avoid GQDs dissociating from the surface of BiVO_4 nanowires. Similarly, different weight percentages of GQDs on BiVO_4 , including 0.5, 2.0, 3.0, 5.0 wt%-GQD/ BiVO_4 nanowire composites were synthesized with various according concentrations of GOD solutions via the procedure above, respectively. To compare with the photocatalytic activities of GQD/ BiVO_4 , grapheme sheet (GS)/ BiVO_4 nanoribbons were also prepared (details in SI).

2.3. Characterization

Transmission electron micro-scope (TEM) and high resolution transmission electron microscopy (HRTEM) observations were performed on a JEOL JEM-2010F electron microscope operating at 200 kV. UV-vis absorption spectra were recorded at room temperature on a Hitachi 3100 spectrophotometer. X-ray diffraction (XRD) patterns were obtained with a Rigaku 18 KW D/max-2550 using Cu Ka radiation. Raman spectra were recorded on a Renishaw in plus laser Raman spectrometer with $\lambda_{\text{exc}} = 633 \text{ nm}$. X-Ray photo-electron spectrometer (XPS) was collected using a Kratos Axis Ultra DLD X-ray photoelectron spectrometer.

2.4. Photocatalytic tests

The photodegradation of CBZ was carried out by adding 0.01 g of photocatalyst in 50 mL of 10 mg L $^{-1}$ CBZ solution at room temperature. The solar irradiation was simulated by using a 350 W Xenon lamp, whose relative intensity is similar to that of natural-light (Fig. S1). Prior to illumination, the suspension was protected from light and magnetically stirred for 1 h to reach adsorption equilibrium, then stirred under visible light all the time. A small amount of suspension (about 1 mL) was taken out every 30 min and filtered through a 0.22 μm microporous membrane. CBZ concentrations in aqueous solutions were quantified by high-performance liquid chromatography (HPLC) at a certain time interval.

2.5. Electrochemical measurements

The cyclic voltammetry (CV) was performed by using a conventional three-electrode system on a CHI 660D electrochemical workstation (Chenhua Instrument, Shanghai, China), which consists of a GQD coated platinum sheet as the working electrode, a platinum wire as the counter electrode, and an Ag/AgCl (saturated KCl) as the reference electrode. CV was recorded in acetonitrile containing 0.1 M TBAPF $_6$ as the supporting electrolyte. The lowest unoccupied molecular orbital (LUMO) energy level in eV as well as the electrochemical energy gap (Eg in eV) of the GQDs was calculated according to the following equation:

$$E_{\text{LUMO}} = -e(E_{\text{red}} + 4.4)$$

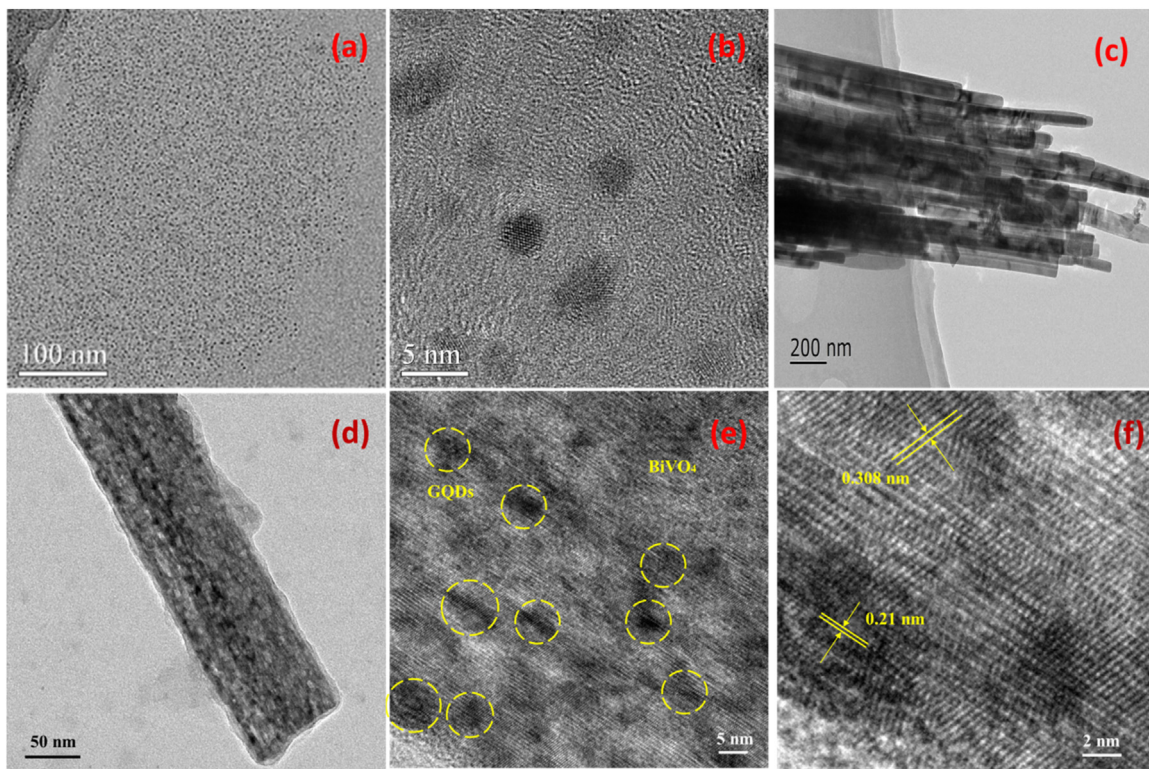


Fig. 1. Low magnification (a) and high magnification (b) SEM images of GQDs. TEM (c), (d) and HRTEM (e), (f) images of 1 wt%-GQD/BiVO₄ heterostructures.

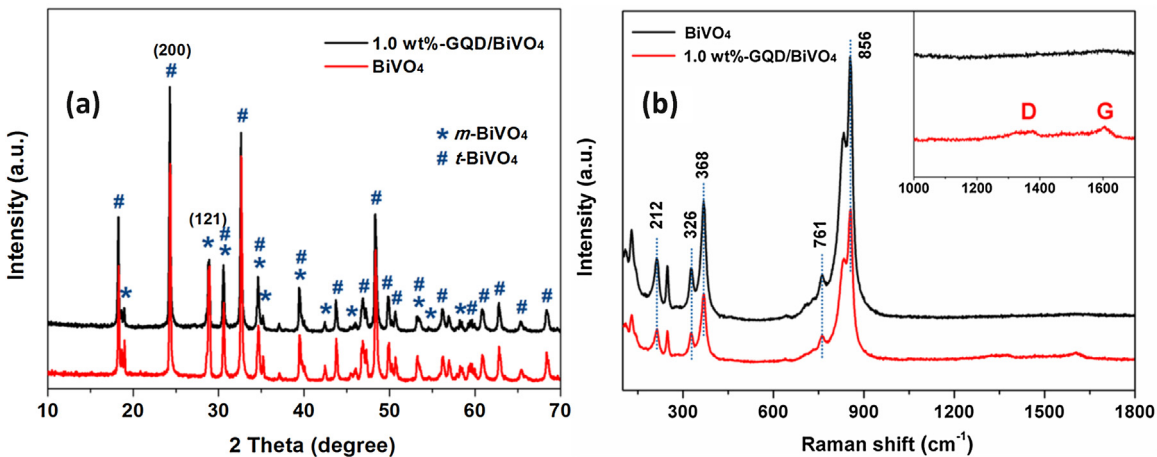


Fig. 2. XRD (a) and Raman (b) spectra of BiVO₄ heterostructures and 1.0 wt%-GQD/BiVO₄ heterojunctions.

2.6. Analytic procedures

2.6.1. HPLC and LC-MS/MS analysis

The HPLC analytical methods used for determining CBZ residues in solutions are detailed in previous work [32]. A high performance liquid chromatography (HPLC, Agilent 1200 series) consisted of C₁₈ column (150 mm × 4.6 mm) and an auto-sampler with 10 μ L volume injection. It was used to monitor the change of CBZ concentration at 230 nm by a VWD detector. The mobile phase was a mixture of methanol and water (55:45, v:v) at rate of 1.0 mL min⁻¹.

A high performance LC-MS/MS (6460 Triple Quad LC-MS/MS, Agilent), which consists of an Agilent 1260 LC chromatograph coupled to an Agilent 6460 mass spectrometer with an electrospray ionization (ESI) interface and a heated nebulizer, were employed to identify the intermediates formed from photocatalytic degrada-

tion of CBZ. A Poroshell 120, 100 × 3 mm EC-C₁₈ end-capped column (2.7 μ m particle size) was used, at the flow rate of 0.4 mL min⁻¹. The injection volume was 10 μ L. The mobile phase was a mixture of acetonitrile (A) and 0.1% formic acid in water (B); the gradient was operated from 5% to 95% A for 8 min, from 95% to 100% A for 2 min, held at 100% for 2 min, and back to the initial conditions in 3.5 min. Mass spectrometry full scanning analysis was performed in the range of 50–500 m/z . The positive electrospray ionization (ESI (+)) operating conditions of the source were as follows: capillary voltage, 4000 V; nebulizer pressure, 40 psi; drying gas flow, 8 mL min⁻¹ at a temperature of 300 °C; nozzle voltage, 0 V.

2.6.2. Total organic carbon (TOC) analysis

TOC was also determined to explore the mineralization level of CBZ during the photocatalytic processes. TOC was systemat-

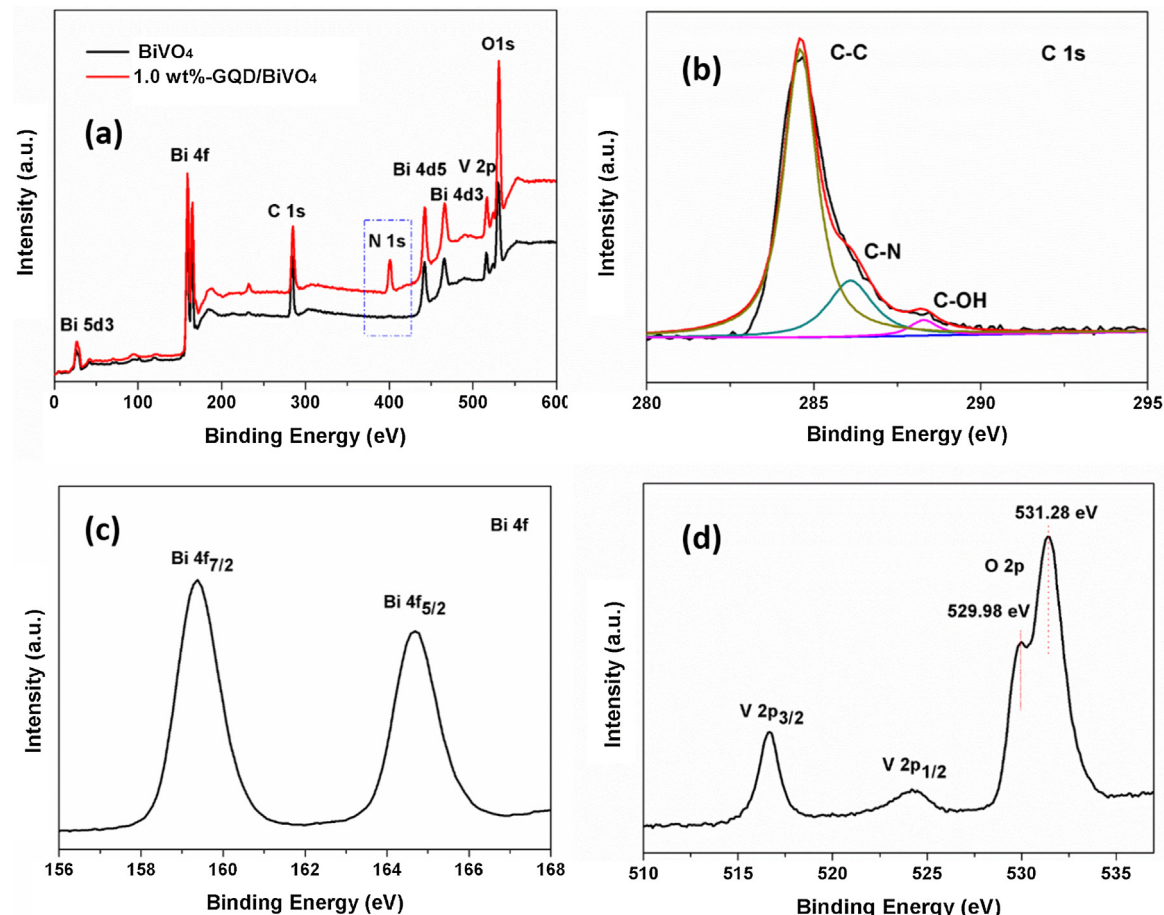


Fig. 3. XPS spectrum of BiVO_4 and 1.0 wt%-GQD/ BiVO_4 heterojunctions (a), C 1s spectrum (b), Bi 4f spectrum (c) and O 1s and V 2p spectrum (d) of 1.0 wt%-GQD/ BiVO_4 heterojunctions.

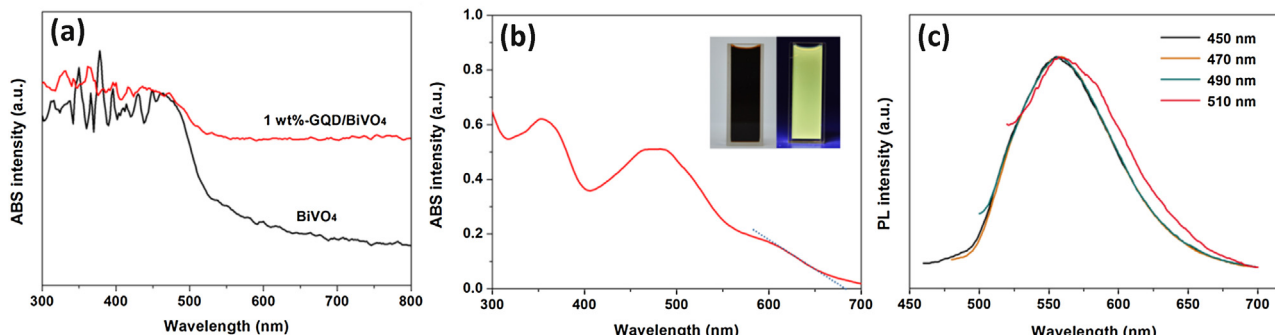


Fig. 4. UV-vis absorption spectra of BiVO_4 and 1.0 wt%-GQD/ BiVO_4 heterojunctions (a), UV-vis absorption spectrum of GQD solution (inset: the photographs of the GQD aqueous solution under visible light and 365 nm UV light) (b), excitation-dependent PL spectra of colloidal GQDs in water (c).

ically monitored using a TOC-VCPN analyzer (Shimadzu, Japan) with the combustion-infrared method. Herein, CBZ or its degradation intermediates were combusted and converted to CO_2 , which was detected and measured by a non-dispersive infrared detector (NDIR). Reproducible TOC values were always obtained using the standard NPOC (Non Purgeable Organic Carbon) method. Herein, the mineralization degree of CBZ was evaluated as the value of TOC/TOC_0 .

2.7. Statistical analyses

Interaction of multi-factors was performed using Design Expert version 8.0 (State Ease, Inc.). The experimental variables studied including initial CBZ concentration (A), catalyst dose (B) and pH (C). Variable ranges were specified based on the preliminary experiments and experimental set-up. The response factor (Y) was defined as the degradation percentage of CBZ after 180 min of photocatalytic reaction.

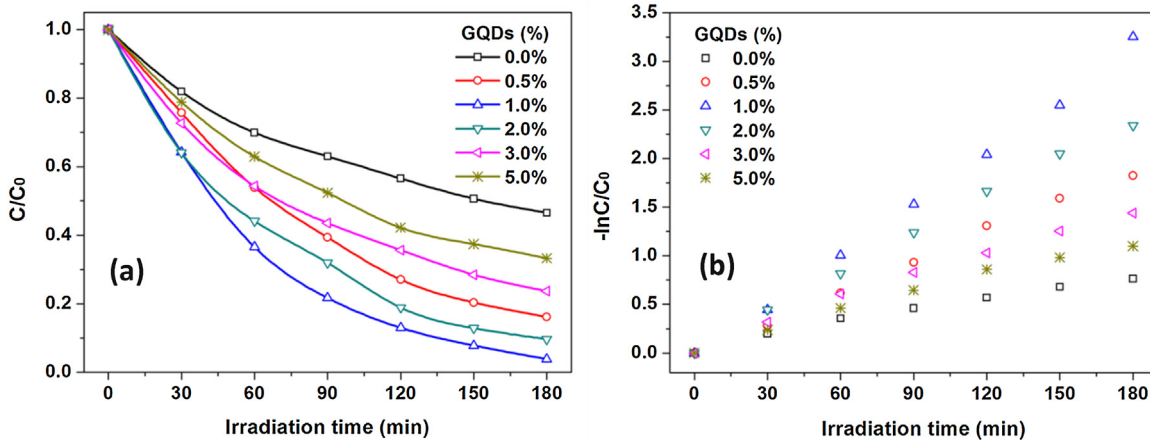


Fig. 5. Effect of different GQD content loading catalysts on CBZ degradation under simulated solar light irradiation. Time-course variation of C/C_0 of CBZ solution (a) and pseudo-first order kinetics for the degradation of CBZ (b).

2.8. Computational methods

The B3LYP method in the framework of density functional theory (DFT) is employed to analyze the reaction mechanisms of CBZ decomposition initiated by $\cdot\text{OH}$. To consider the solvent effect, the single point calculations were performed at the B3LYP/6-31+G(d,p) level, and the solvent is water. All calculations were carried out with the Gaussian 09 software package.

3. Results and discussion

3.1. Characterization of GQD/BiVO₄ hybrid catalyst

The morphology of the GQDs was examined by TEM (Fig. 1a and b). Their TEM image showed that the GQDs were well dispersed with uniform lateral sizes. The interlayer spacing was 3.34 Å, which was determined by XRD (Fig. S2a). The Raman spectrum (Fig. S2b) showed a D band at 1368 cm⁻¹ and a stronger G band at 1587 cm⁻¹. The detailed microstructures of 1.0 wt% GQD/BiVO₄ (the highest photocatalytic activity for CBZ degradation) were characterized by TEM (Fig. 1c and d), which presented uniform nanoribbons. The high-magnification image (Fig. 1e) clearly showed some small GQD particles adhering to the surface of the individual BiVO₄ nanoribbon, suggesting that GQD nanoparticles were uniformly anchored on the nanoribbons. Further details of the morphology were provided in the TEM image in Fig. 1f. The HRTEM showed the interplanar space which was measured as 0.21 nm was in agreement with the d-spacing of graphene (100) planes, and the substrate was regarded as BiVO₄ which was confirmed by the interplanar spacing of 0.308 nm [33,34], implying the formation of the GQD/BiVO₄ heterostructures was accomplished.

The X-ray diffraction (XRD) patterns indicated that as-prepared BiVO₄ heterostructures were composed of both monoclinic BiVO₄ crystalline phase [*m*-BiVO₄, JCPDS no. 014-0688] and tetragonal BiVO₄ crystalline phase [*t*-BiVO₄, JCPDS no. 014-133] (Fig. 2a). The characteristic diffraction peaks appeared at 28.8° and 24.5° were accordance with *m*-BiVO₄ and *t*-BiVO₄, respectively. Raman spectra of the BiVO₄ and GQD/BiVO₄ samples shown in Fig. 2b also suggested the existence of monoclinic/tetragonal heterostructures for BiVO₄. The pure BiVO₄ exhibited five Raman shifts at 208 cm⁻¹, 329 cm⁻¹, 365 cm⁻¹, 710 cm⁻¹ and 826 cm⁻¹, corresponding to the external rotation mode, the symmetric bending mode δS (VO₄) and the asymmetric bending mode δas (VO₄), the asymmetric V–O stretching mode Vas (V–O) and the symmetric V–O stretching mode δS (V–O), respectively, which were consistent with those

reported in previous papers [35,36]. However, our samples with or without GQD sensitization both clearly illustrated the main peak shifts to 856 cm⁻¹, implying transition from monoclinic to tetragonal occurred [37]. In the meanwhile, compared with BiVO₄ heterostructures, two additional peaks at 1587 and 1369 cm⁻¹ were observed for GQD/BiVO₄ heterojunctions in Fig. 2b, confirming the GQDs have loaded on the surface of BiVO₄ heterostructures.

Besides, the chemical composition and bonding configuration of the as-prepared hybrids were analyzed by XPS (Fig. 3). As shown in Fig. 3a, the peaks of Bi, C, V and O were found in both BiVO₄ and GQD/BiVO₄ composites. The presence of C was likely attributed to the adventitious elemental carbon on the surface of the sample, or the carbon tape used by the XPS technique [38]. Moreover, the N1s signal was only observed in GQD/BiVO₄ composites which could be attributed to GQDs. Apart from the strong signal of C–C (284.7 eV), the C–NH₂ (286.1 eV) and C–OH (288.4 eV) signals in Fig. 3b were also detected, which is corresponding with the C 1s spectrum of GQDs in our previous studies and certainly confirms the presence of GQDs on the surface of the sample. From the Bi 4f spectrum of GQD/BiVO₄ composites (Fig. 3c), two peaks at approximately 159.1 and 164.4 eV could be assigned to the binding energies of Bi 4f_{7/2} and Bi 4f_{5/2}, respectively [39].

In order to elucidate the strengthened optical properties by GQDs, the hybrids were subjected to analysis of UV–vis absorption spectra. UV–vis absorption spectra of BiVO₄ heterostructures in Fig. 4a demonstrated that BiVO₄ exhibited significantly optical absorption from UV light to visible light region (about 600 nm); however, there was no substantial absorption band from 600 to 800 nm, involving the transition of trap states of intrinsic defects within the bandgap. Contrarily, GQD/BiVO₄ heterojunctions exhibited strong spectral response in both the UV and the visible region. That was attributed to the narrow bandgap of GQDs, which showed good yellow fluorescence properties under the 365 nm UV light irradiation in the inset of Fig. 4b. The GQDs emitted strong photoluminescence (PL) from green to yellow (Fig. 4c), was well confined, nearly irrespective of excitation wavelength. In addition, from the plot of $(\text{Ahv})_{1/2}$ vs energy $h\nu$ in Fig. S3, the band gap energy (E_g) estimated from the onset of the curve edges are calculated to be about 2.1 and 2.03 eV for BiVO₄ nanoribbon and 1.0 wt% GQD/BiVO₄ nanoribbon composite, respectively. The relatively narrow band-gap energy observed for 1.0 wt% GQD/BiVO₄ nanoribbon composite may be ascribed to the strong interaction in the hybrid structure, which makes the utilization of the solar spectrum more efficient. The improved light absorption could therefore excite more photogenerated carriers from the GQD/BiVO₄ hetero-

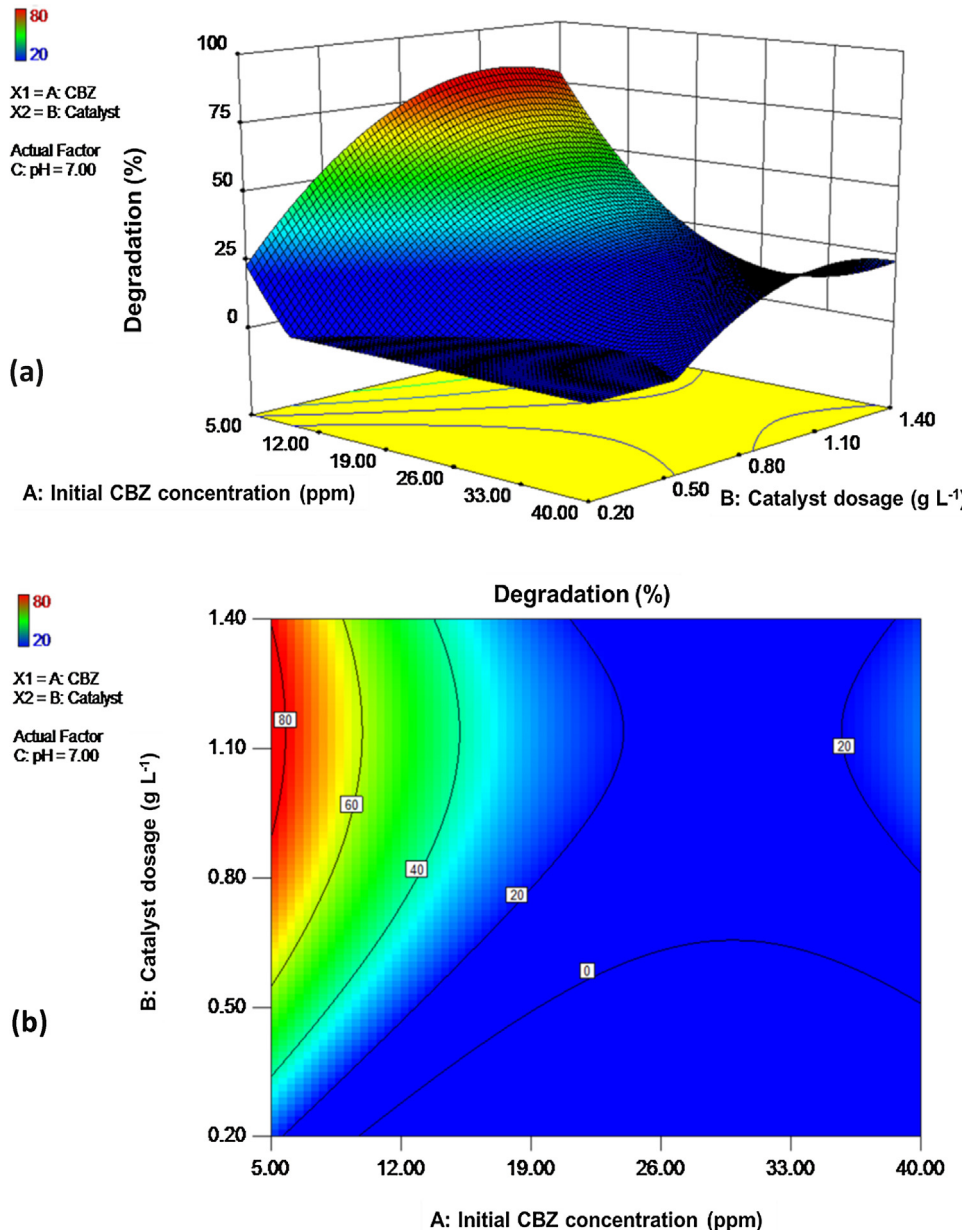


Fig. 6. Response surface (a) and two-dimension contour plots (b) for interaction between initial CBZ concentration (A) and catalyst dosage (B). Experimental conditions: pH = 7, at room temperature.

junctions to decontaminate the pollutants, which would improve the practical application under natural solar light [40].

3.2. Photocatalytic activity

To examine the effects of GQDs on the photocatalytic capacity, six categories of heterojunctions, 0, 0.5, 1.0, 2.0, 3.0 and 5.0 wt%-GQD/BiVO₄ catalysts were used. As shown in Fig. 5a, the degradation efficiency of GQDs loading BiVO₄ were higher than that of binary BiVO₄ heterostructures, the latter only reached a degradation rate of 53.5% after 180 min illumination. Obviously, GQDs exhibited a positive effect on the degradation efficiency of CBZ, which could sensitize the photocatalytic capacity of BiVO₄ to enhance the degradation efficiencies. With the catalysis of 0.5 and 1.0 wt%-GQD/BiVO₄, the degradation rates of CBZ could be achieved as 83.9% and 96.1%, respectively. However, the degradation efficiency did not strictly grow over the increase of GQD content on

BiVO₄. Further increasing GQD contents to 2.0, 3.0 and 5.0 wt%, the catalytic degradation of CBZ seemed to be impeded, which could be attributed to the excess GQDs might cover up the active sites on the surface of BiVO₄, hence reducing the catalytic capacity [41]. Meanwhile, the photocatalytic properties of 1.0 wt%-GQD/BiVO₄ composite were better than the similarly loaded GS/BiVO₄ composite (Fig. S4a). There was almost no degradation effect with the latter one, since larger GSs attaching on the surface of BiVO₄ hindering the visible-light absorption of BiVO₄. The UV-vis absorption spectra of GS/BiVO₄ composite were illustrated in Fig. S4b.

Fig. 5b illustrated the degradation kinetics of CBZ in the presence of BiVO₄ with various GQD contents. The excellent linear fits of experimental data suggested that the CBZ degradation was followed pseudo first-order kinetics under all categories of GQD/BiVO₄ heterojunctions in aqueous solutions. The rate constant *k* and the coefficient of determination *R*² for the kinetics of CBZ were given in Table S1. As expected, 1.0 wt%-GQD/BiVO₄ showed the

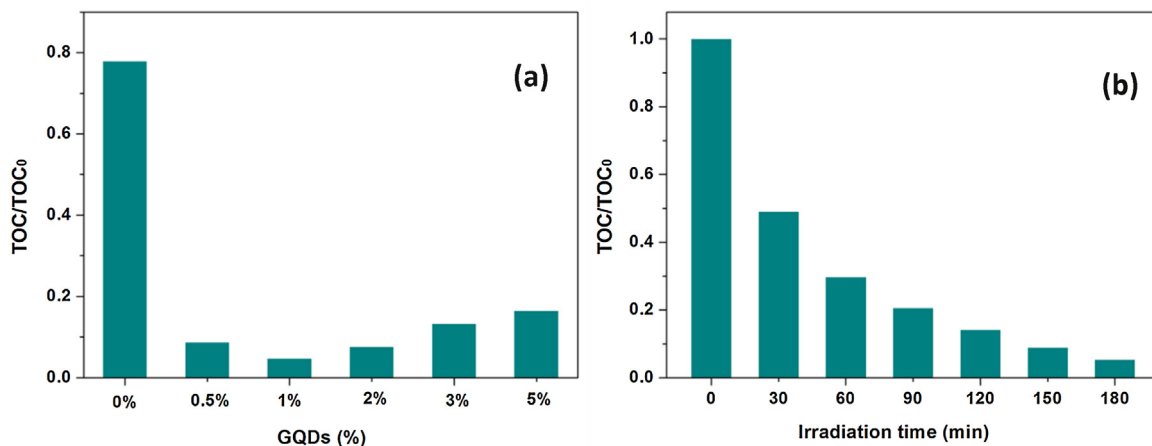


Fig. 7. Mineralization degree of CBZ with catalysts loaded various GQD contents after 180 min irradiation (a) and 1.0 wt%-GQD/BiVO₄ heterojunctions within 180 min irradiation (b). Experimental conditions: [CBZ]₀ = 5 ppm, pH = 7, at room temperature.

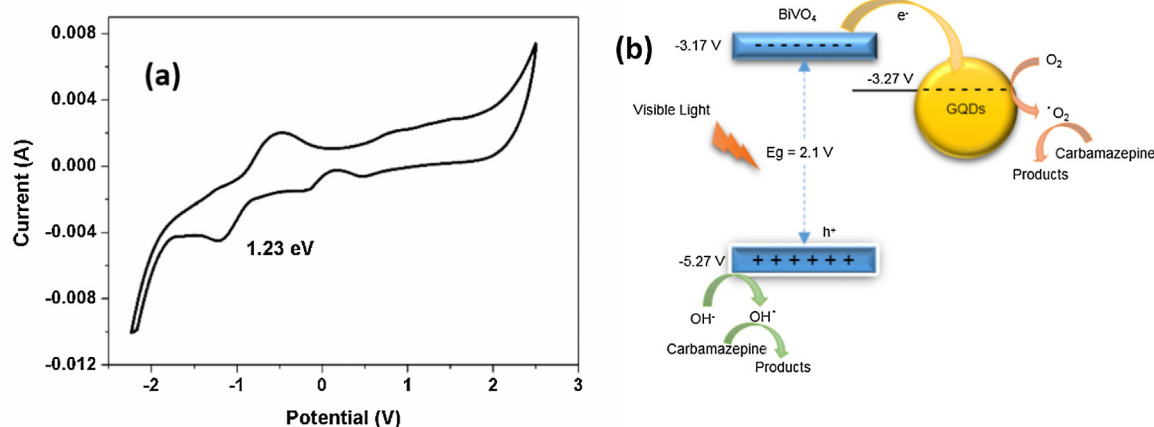


Fig. 8. CV curve of BiVO₄ nanoribbons (a). Diagrams of energy position and photogenerated electron-hole pairs transfer of GQD/BiVO₄ nanoribbons under simulated solar light irradiation (b).

highest *k* value which was 4 times more than that of catalyst without GQDs, implying the best photocatalytic degradation rate could be obtained with this catalyst. Thus, 1.0 wt%-GQD/BiVO₄ catalysts were chosen to accomplish the following studies.

The condition parameters, such as initial contaminant concentration, catalyst dosage and pH, affect catalytic degradation intensively [42]. Herein, the effects of these individual parameters on CBZ degradation performance were investigated separately. As expected, while fixing two parameters and varying the other one parameter, the degradation characteristic of CBZ was changing accordingly. The degradation efficiency was preferable when adjusting initial CBZ concentration lower. This is reasonable, since limited active sites and substances on catalysts could just burden a certain amount of target contaminants at a certain given time. Besides, addition of an appropriate amount of catalysts was also important. When initial CBZ concentration and pH were set as 5 ppm and 7, respectively, the best degradation efficiency was accomplished with 1.0 g L⁻¹ of catalysts. Moreover, the best catalytic property was found when the pH was close to neutral (pH = 7), either acidic or alkaline condition could hinder the degradation of CBZ. This phenomenon suggested the present catalyst was suitable for the practical applications.

In the practical process, multi-factors always influence the degradation process together. In this light and in order to evaluate the combined effects and interactions of the conditions above, the three-dimensional (3D) response surface graph and two-

dimension (2D) contour plot of the degradation of CBZ are plotted in Fig. 6. Based on the values of independent variables coefficients in the regression model, the order in which the studied variables affect the response was: initial CBZ concentration (A) > catalyst dosage (B) > pH (C). As shown in Fig. 6a, the shape of the response surface curves described the interactions between the first two important factors, A (initial CBZ concentration) and B (catalyst dosage). The results visually demonstrated a decrease of the initial CBZ concentration increased the degradation efficiency. For the practical guidance to treat for wastewater containing CBZ, diluting the water and adopting appropriate amount of catalysts could achieve a preferable treatment performance. Moreover, the photocatalytic activity of GQD/BiVO₄ heterostructures for CBZ was compared with those reported in other studies (Table S2). The results displayed that GQD/BiVO₄ heterostructures prepared in this study was an efficient and rapid photocatalyst towards CBZ.

3.3. Evaluation of CBZ mineralization

Although BiVO₄ heterostructures sensitized by GQDs could significantly improve the decomposition of CBZ as discussed above, the mineralization degree of CBZ during the photocatalytic processes should be elucidated as well. Herein, TOC remains in solutions after illumination were determined to access the mineralization course.

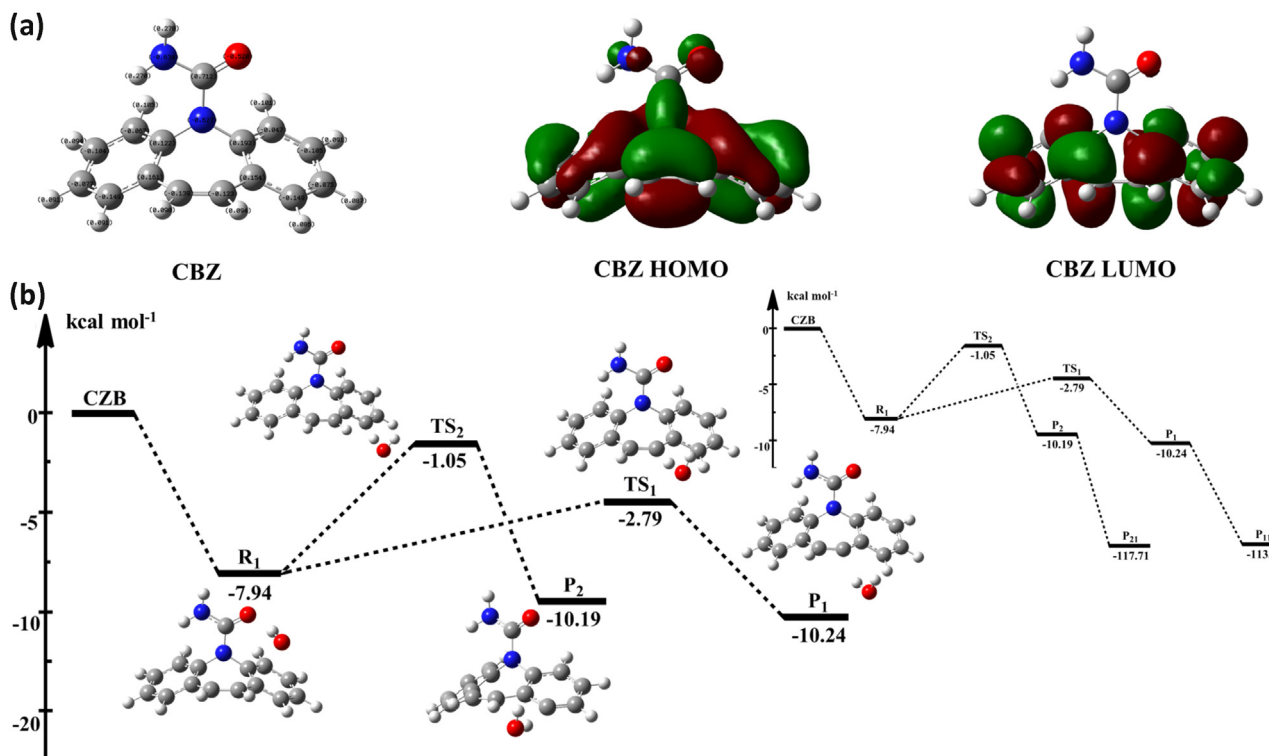


Fig. 9. Optimized of structure of CBZ at the B3IYP/6-31G(d,p) level (a). (The gray, white, red and blue balls represent the carbon, hydrogen, oxygen and nitrogen atoms, respectively.) Profile of the potential energy surface for the initial step reaction of CBZ with •OH (b). (Inset: the framework about two different categories of possible reaction channel.). (For interpretation of the references to colour in this figure legend, the reader is referred to the web version of this article.)

As depicted in Fig. 7a, the additive of GQDs could not only lift the degradation efficiency, but also carry the TOC decay forward, in other words, improve the mineralization degree of CBZ. Surprisingly, the mineralization profiles with different catalysts were corresponding to the degradation efficiency. Binary BiVO₄ hybrids without GQD sensitization displayed the lowest mineralization capacity (TOC/TOC₀ = 0.78), while 1.0 wt%-GQD/BiVO₄ exhibited the greatest mineralization performance among all the catalysts (TOC/TOC₀ = 0.05). It has been proven that carbon quantum dots could not only harvest the broad wavelength light, but also facilitate the separation of electrons and holes, hinder the re-combination [43,44]. Thus, there are enough reasons to believe that the existence of GQDs may not only strongly enlarge the visible-light absorption of BiVO₄ but also enable BiVO₄ obtain high photocatalytic activity for CBZ removal.

With the catalytic activity of 1.0 wt%-GQD/BiVO₄, TOC residues in CBZ solution gradually decreased along with irradiation time (Fig. 7b). The mineralization in terms of TOC removal achieved under visible light was 51.0%, 70.3%, 79.4%, 85.8% and 91.1% with 30, 60, 90, 120 and 150 min illumination, respectively. After 180 min illumination, CBZ was almost completely mineralized (>95% TOC decay). It could be inferred that CBZ could be completely degradation with less residues of transformation products formed during the photocatalytic process.

3.4. Improved photocatalytic mechanism

The photocatalytic results have shown the excellent photoactivity of the GQD doped BiVO₄ nanoribbons on the degradation of CBZ. To understand these enhancement effects induced by the GQDs, we measured the CV curve of GQDs and BiVO₄ nanoribbons to determine their LUMO and CB, respectively. From the reduction potential (E_{red}) of -1.13 V vs. SCE, the LUMO energy level relative to the vacuum level was calculated to be -3.27 eV using the equa-

tion in experimental section, which were detailed in previous work [30]. At the same times, the CB energy level of BiVO₄ nanoribbons was calculated to be -3.17 eV in Fig. 8a. It was noted that the LUMO energy level was lower than the CB bottom of the BiVO₄ nanoribbons, which indicated that the electronic transfer from the BiVO₄ nanoribbons to GQDs has taken place when the BiVO₄ nanoribbons absorbed by visible light, as demonstrated in Fig. 8b. It was thus expected that effective separation of photoexcited electrons from holes in the BiVO₄ nanoribbons, and the fast injection of the electrons to the GQD LUMO. Those holes can be left on the surface of the BiVO₄ nanoribbons to further oxidize water producing •OH free radicals, which would eventually decompose organic pollutants in water into CO₂ and H₂O [45,46]. Based on all of the above experiments and analyses, the GQD doped BiVO₄ nanoribbon photocatalyst played a beneficial role in improving charge separation and photocatalytic performance.

3.5. Byproducts identification and degradation mechanism

To further elucidate the degradation pathway and clarify the photocatalytic mechanisms, unknown transformation products (TPs) were identified via LC-MS/MS spectra obtained within the whole reaction period of CBZ. Table S3 summarized the information of ten tentatively identified TPs without authentication. A great portion of these identified TPs were also detected in other studies [32,47–49], which were carried out by other AOPs initiated with •OH radicals, implying these radicals might be also the predominant reaction catalytic active species. Furthermore, the results of quenching experiments on h⁺, •O²⁻ and •OH with ammonium oxalate (AO), benzoquinone (BQ), and isopropanol (IPA) confirmed with the conjecture that •OH was the major contributor to the photocatalytic degradation of CBZ herein (Fig. S5). Noteworthily, two isomers with the molecular mass of 252 (TP/252-1 and 252-2) were identified as the products formed from hydrogen abstraction of het-

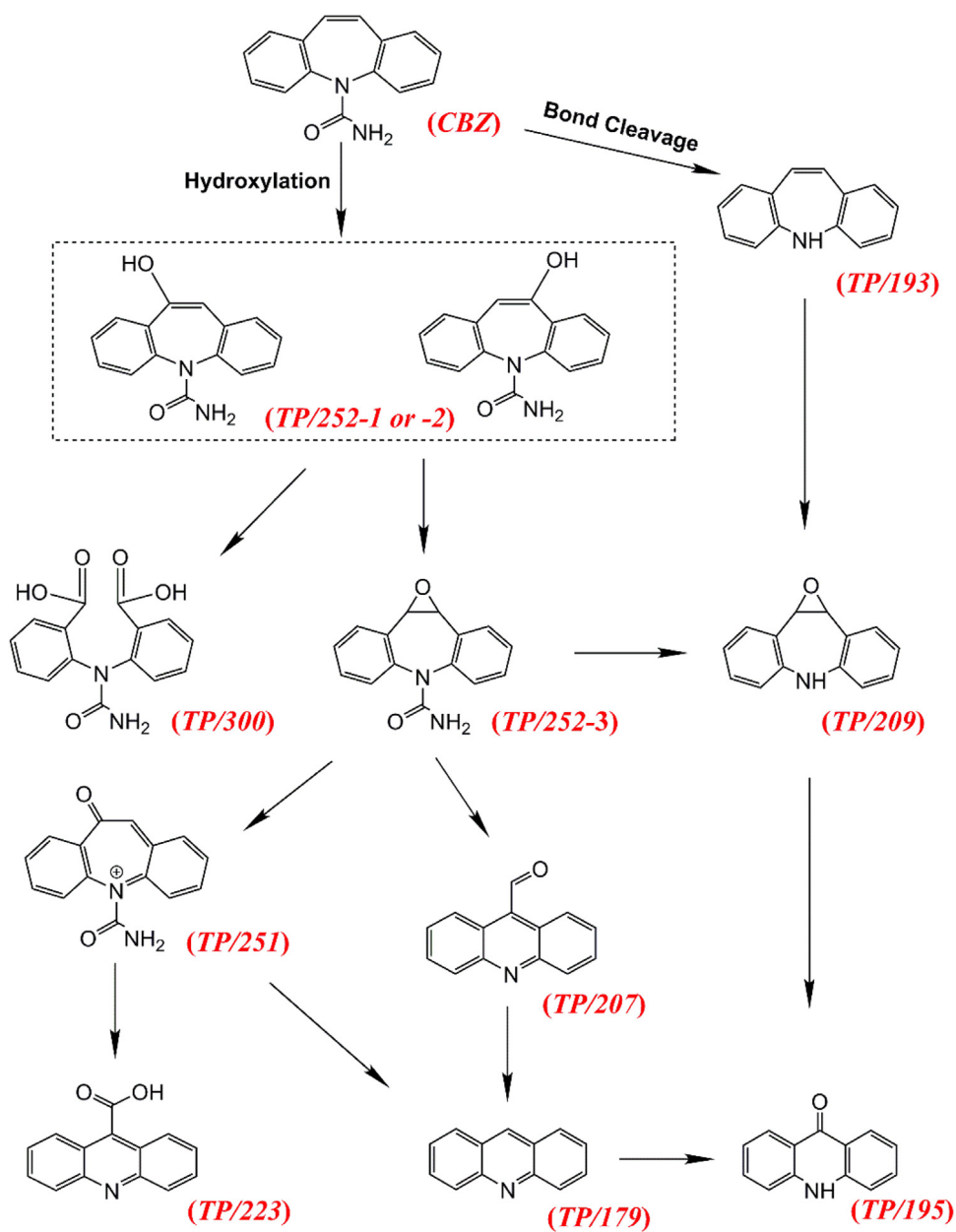


Fig. 10. Schematic illustration of proposed CBZ degradation pathways by simulated solar induced photocatalysis with GQD/BiVO₄ hybrids.

erocycle, rather than those from aromatic ring, since the energy barrier of the latter reaction ($-1.05 \text{ kcal mol}^{-1}$) were calculated much higher than those of the former ($-2.79 \text{ kcal mol}^{-1}$) (Fig. 9).

Based on the spectra of individual TP before, during, and after the light illumination, time variation profiles of TPs during the photocatalytic reaction were depicted in Fig. S6. As shown in Fig. S6, peak areas of CBZ consistently decreased over the irradiation time, suggesting CBZ was efficiently decomposed by photocatalysis; meanwhile, some TPs were formed swiftly within 30 min irradiation, such as TP/252-1 and 252-2, and decomposed after 60 min irradiation. Interestingly, TP/300 was massively formed after 60 min in accordance with the decomposition of TP/252-1 and 252-2, implying TP/300 might be the decomposition product of these isomers. On the other hand, a part of lower-molecular TPs, for instance, TP/179, 195, were generated gently with the irradiation duration. These TPs could be regarded as the identified terminal organic transformation products before carboxylation and complete mineralization, since a portion of these TPs degraded into

carboxyl compounds and a certain amount of these TPs would be continually generated, which could maintain the amount of TP/179, 195 relatively constant at a time.

Based on the tentatively identified TPs, as well as the evolution properties of individual TPs, the degradation pathways of CBZ under the photocatalysis of GQD/BiVO₄ hybrids were proposed in Fig. 10. As illustrated in the proposed pathways, CBZ could be firstly suffered two potential paths to form diverse TPs, as hydroxylated products TP/252-1 and 252-2, product loss an amide group from CBZ TP/193. These phenomena suggested the main initial degradation pathways of CBZ with the hybrid catalysts involved the following steps: (1) hydrogen abstraction and hydroxylation of heterocycle ring; (2) cleavage of the amide group. The relative pathways occurred via strongly oxidative attack from •OH generated by photo-excited heterostructural catalysts, which was consistent with the previous studies that induced by photocatalysis with catalysts [50–53]. With the proceeding reactions, epoxidation of heterocycle and heterocycle ring-open might occur. Under the

attack from $\cdot\text{OH}$, CBZ was eventually degraded into smaller organic fragments and mineralized to CO_2 and H_2O .

4. Conclusions

In the present study, GQDs with yellow fluorescence were fabricated with binary BiVO_4 to form a novel heterostructures GQD/ BiVO_4 , which were then applied to treat with an environmentally recalcitrant drug, carbamazepine (CBZ). The characterization for GQD/ BiVO_4 illustrated that the ternary heterostructures were well fabricated and GQDs were dispersed on BiVO_4 . The research focusing on the CBZ degradation demonstrated GQDs on BiVO_4 could prompt the degradation of CBZ, however, the best degradation performance could be just achieved with an appropriate amount of GQDs. Herein, 1.0 wt% GQDs on BiVO_4 was the optimal situation. Significantly, relatively complete mineralization (>95%) of CBZ could be obtained with 1.0 wt% GQD/ BiVO_4 after 180 min. Within the degradation process, the parameters such as initial CBZ concentration, catalyst dosage and pH affected intensively, and these variables affected the degradation rate in descending order was initial CBZ concentration > catalyst dosage > pH. The radical scavenger experiments elucidated $\cdot\text{OH}$ was the predominant species in the CBZ photocatalytic degradation process. Based on the identified intermediates and theoretical calculations, we confirmed that the heterocycle of CBZ, rather than aromatic ring, was susceptible to the attack from $\cdot\text{OH}$. As a consequence, the potential degradation pathways of CBZ were proposed according to the results and conclusions above.

Acknowledgements

This work has been supported by National Natural Science Foundation of China (No. 41573096, 21671129, 21571124, 51472241), the Shanghai Sailing Program (No. 16YF1404400), the Major State Basic Research Development Program of China (No. 2011CB933402), Program for Changjiang Scholars and Innovative Research Team in University (No. IRT13078).

Appendix A. Supplementary data

Supplementary data associated with this article can be found, in the online version, at <http://dx.doi.org/10.1016/j.apcatb.2016.10.067>.

References

- [1] M.A. Shannon, P.W. Bohn, M. Elimelech, J.G. Georgiadis, B.J. Marinas, A.M. Mayes, *Nature* 452 (2008) 301–310.
- [2] T. Ternes, A. Joss, J. Oehlmann, *Water Res.* 72 (2015) 1–2.
- [3] A. Alsbaee, B.J. Smith, L. Xiao, Y. Ling, D.E. Helbling, W.R. Dichtel, *Nature* (2015).
- [4] R. Banaschik, P. Lukes, H. Jablonowski, M.U. Hammer, K.D. Weltmann, J.F. Kolb, *Water Res.* 84 (2015) 127–135.
- [5] X. Garcia-Santiago, A. Franco-Uria, F. Omil, J.M. Lema, *J. Hazard. Mater.* 302 (2016) 72–81.
- [6] Y. Zhang, S.U. Geissen, C. Gal, *Chemosphere* 73 (2008) 1151–1161.
- [7] A. Carabin, P. Drogui, D. Robert, J. *Taiwan Inst. Chem. Eng.* 54 (2015) 109–117.
- [8] A. Joss, E. Keller, A.C. Alder, A. Gobel, C.S. McArdell, T. Ternes, H. Siegrist, *Water Res.* 39 (2005) 3139–3152.
- [9] N. Vieno, T. Tuukkanen, L. Kronberg, *Water Res.* 41 (2007) 1001–1012.
- [10] Z. Xie, G. Lu, J. Liu, Z. Yan, B. Ma, Z. Zhang, W. Chen, *Chemosphere* 138 (2015) 140–147.
- [11] R. Gurke, M. Rossler, C. Marx, S. Diamond, S. Schubert, R. Oertel, J. Fauler, *Sci. Total Environ.* 532 (2015) 762–770.
- [12] S. Matongo, G. Birungi, B. Moodley, P. Ndungu, *Environ. Sci. Pollut. Res. Int.* 22 (2015) 10298–10308.
- [13] B. Lopez, P. Ollivier, A. Togola, N. Baran, J.P. Ghemest, *Sci. Total Environ.* 518–519 (2015) 562–573.
- [14] D.P. Mohapatra, S.K. Brar, R.D. Tyagi, P. Picard, R.Y. Surampalli, *Talanta* 99 (2012) 247–255.
- [15] E. De Laurentiis, S. Chiron, S. Kouras-Hadef, C. Richard, M. Minella, V. Maurino, C. Minerio, D. Vione, *Environ. Sci. Technol.* 46 (2012) 8164–8173.
- [16] W. Li, V. Nanaboina, Q. Zhou, G.V. Korshin, *Water Res.* 46 (2012) 403–412.
- [17] O.S. Keen, S. Baik, K.G. Linden, D.S. Aga, N.G. Love, *Environ. Sci. Technol.* 46 (2012) 6222–6227.
- [18] C. Sichel, C. Garcia, K. Andre, *Water Res.* 45 (2011) 6371–6380.
- [19] V. Naddeo, S. Meric, D. Kassinos, V. Belgiorio, M. Guida, *Water Res.* 43 (2009) 4019–4027.
- [20] D.P. Mohapatra, S.K. Brar, R.D. Tyagi, P. Picard, R.Y. Surampalli, *Sci. Total Environ.* 470–471 (2014) 58–75.
- [21] D. Deng, K.S. Novoselov, Q. Fu, N. Zheng, Z. Tian, X. Bao, *Nat. Nanotechnol.* 11 (2016) 218–230.
- [22] Y. Yan, J. Miao, Z. Yang, F.X. Xiao, H.B. Yang, B. Liu, Y. Yang, *Chem. Soc. Rev.* 44 (2015) 3295–3346.
- [23] Y.Q. Yang, H.X. Li, F.L. Hou, J.Y. Hu, X.D. Zhang, Y.X. Wang, *Mater. Lett.* 180 (2016) 97–100.
- [24] W. Yin, W. Wang, L. Zhou, S. Sun, L. Zhang, *J. Hazard. Mater.* 173 (2010) 194–199.
- [25] L. Hu, S. Dong, Y. Li, Y. Pi, J. Wang, Y. Wang, J. Sun, *J. Taiwan Inst. Chem. Eng.* 45 (2014) 2462–2468.
- [26] O.F. Lopes, K.T.G. Carvalho, A.E. Nogueira, W. Avansi, C. Ribeiro, *Appl. Catal. B: Environ.* 188 (2016) 87–97.
- [27] X. Lang, J. Zhao, X. Chen, *Angew. Chem.* 55 (2016) 4697–4700.
- [28] M.H. Rasoulifard, M.S. Seyed Dorraji, A.R. Amani-Ghadim, N. Keshavarz-babaeinezhad, *Appl. Catal. A: Gen.* 514 (2016) 60–70.
- [29] X. Zhang, Y. Wang, F. Hou, H. Li, Y. Yang, X. Zhang, Y. Yang, Y. Wang, *Appl. Surf. Sci.* 391 (2017) 476–483.
- [30] Z.D. Lei, J.J. Wang, L. Wang, X.Y. Yang, G. Xu, L. Tang, *J. Hazard. Mater.* 312 (2016) 298–306.
- [31] L. Wang, Y. Wang, T. Xu, H. Liao, C. Yao, Y. Liu, Z. Li, Z. Chen, D. Pan, L. Sun, M. Wu, *Nat. Commun.* 5 (2014) 5357.
- [32] N. Liu, Z.-D. Lei, T. Wang, J.-J. Wang, X.-D. Zhang, G. Xu, L. Tang, *Chem. Eng. J.* 295 (2016) 484–493.
- [33] C. Lv, G. Chen, J. Sun, Y. Zhou, S. Fan, C. Zhang, *Appl. Catal. B: Environ.* 179 (2015) 54–60.
- [34] S. Gu, W. Li, F. Wang, S. Wang, H. Zhou, H. Li, *Appl. Catal. B: Environ.* 170–171 (2015) 186–194.
- [35] K.-H. Ye, X. Yu, Z. Qiu, Y. Zhu, X. Lu, Y. Zhang, *RSC Adv.* 5 (2015) 34152–34156.
- [36] S. Hernández, G. Gerardi, K. Bejtka, A. Fina, N. Russo, *Appl. Catal. B: Environ.* 190 (2016) 66–74.
- [37] Y. Xue, X. Wang, *Int. J. Hydrogen Energy* 40 (2015) 5878–5888.
- [38] Z. Ai, W. Ho, S. Lee, L. Zhang, *Environ. Sci. Technol.* 43 (2009) 4143–4150.
- [39] S.H. Hsieh, G.J. Lee, C.Y. Chen, J.H. Chen, S.H. Ma, T.L. Horng, K.H. Chen, J.J. Wu, *J. Nanosci. Nanotechnol.* 12 (2012) 5930–5936.
- [40] Y.-n Zhang, H. Tian, G. Zhao, *ChemElectroChem* 2 (2015) 1728–1734.
- [41] D. Pan, C. Xi, Z. Li, L. Wang, Z. Chen, B. Lu, M. Wu, *J. Mater. Chem. A* 1 (2013) 3551.
- [42] P. Hadi, M.H. To, C.W. Hui, C.S. Lin, G. McKay, *Water Res.* 73 (2015) 37–55.
- [43] S.Y. Lim, W. Shen, Z. Gao, *Chem. Soc. Rev.* 44 (2015) 362–381.
- [44] H. Li, X. He, Z. Kang, H. Huang, Y. Liu, J. Liu, S. Lian, C.H. Tsang, X. Yang, S.T. Lee, *Angew. Chem.* 49 (2010) 4430–4434.
- [45] X. Huang, Q. Shen, J. Liu, N. Yang, G. Zhao, *Energy Environ. Sci.* 9 (2016) 3161–3171.
- [46] Y. Zhang, B. Tang, Z. Wu, H. Shi, Y. Zhang, G. Zhao, *Green Chem.* 18 (2016) 2424–2434.
- [47] W.L. Wang, Q.Y. Wu, N. Huang, T. Wang, H.Y. Hu, *Water Res.* 98 (2016) 190–198.
- [48] Y. Rao, H. Yang, D. Xue, Y. Guo, F. Qi, J. Ma, *Ultrason. Sonochem.* 32 (2016) 371–379.
- [49] J.M. Monteagudo, A. Durán, R. González, A.J. Expósito, *Appl. Catal. B: Environ.* 176–177 (2015) 120–129.
- [50] C.S. Kuo, C.F. Lin, P.K. Hong, *Water Res.* 74 (2015) 1–9.
- [51] C.S. Kuo, C.F. Lin, P.K. Hong, J. *Hazard. Mater.* 301 (2016) 137–144.
- [52] G. Zhang, E.M. Wurtzler, X. He, M.N. Nadagouda, K. O'Shea, S.M. El-Sheikh, A.A. Ismail, D. Wendell, D.D. Dionysiou, *Appl. Catal. B: Environ.* 163 (2015) 591–598.
- [53] L. Ismail, A. Rifai, C. Ferronato, L. Fine, F. Jaber, J.-M. Chovelon, *Appl. Catal. B: Environ.* 185 (2016) 88–99.